Eur. Phys. J. D **5**, 207–216 (1999)

THE EUROPEAN PHYSICAL JOURNAL D

EDP Sciences

Photodetachment microscopy of O^-

C. Blondel[a], C. Delsart, F. Dulieu, and C. Valli

Laboratoire Aimé-Cotton, Centre national de la recherche scientifique, bâtiment 505, 91405 Orsay Cedex, France

Received: 5 June 1998 / Accepted: 16 October 1998

Abstract. Photodetachment of O^- ions is performed in the presence of a static electric field. A high spatial resolution electron detector is used to map out the ejected electron's wave function. Propagation over half a metre does not alter the stationary structure the electron wave possesses in the direction orthogonal to the detachment motion. Nodes and antinodes of electron current density are observed, that can be interpreted as direct imaging of the internal atomic wave function. Because detachment of a negative ion can be represented accurately in the free-electron approximation, the obtained images can also be viewed as direct experimental representations of the Green function of the uniform acceleration problem. Agreement of the measured distributions with the exact expression of this wave-function appears quite satisfactory.

PACS. 32.80.Gc Photodetachment of atomic negative ions – 03.75.-b Matter waves – 07.78.+s Electron, positron, and ion microscopes, electron diffractometers, and related techniques

1 An introduction to continuum Lo Surdo-Stark spectroscopy

Modification of the atomic spectra by an external electric field was first experimentally demonstrated on the discrete spectrum of hydrogen [1,2]. For discrete states with a low principal quantum number n, provided that the external electric field F be small when compared to the atomic unit 5.14×10^{11} V m^{-1}, F actually remains small with respect to the mean electric field an atomic electron experiences along its orbit. The modified atomic spectrum can thus be calculated by means of a perturbation theory [3].

Selective excitation of high principal quantum numbers, *i.e.* Rydberg states, has made it possible to prepare relatively loosely bound atoms, for which laboratory electric fields appear as more intense ones. Hydrogen for instance can be selectively excited into individual Lo Surdo-Stark components of a given n manifold [4,5], in order to check theoretical formulae for the state-dependent field-ionisation thresholds [6]. A counter-intuitive result is confirmed, namely that for a given principal quantum number n, the lower the energy sublevel, the higher the ionisation rate.

This remarkable feature reveals an underlying symmetry: even in the presence of both a uniform and a Coulomb electric field, the electron motion remains separable along parabolic coordinates [3,7,8]. Taking the initial position of the atom as the origin of the coordinates, with z the Cartesian coordinate along the uniform electric field direction, $r = \sqrt{x^2 + y^2 + z^2}$ the distance from the origin, parabolic coordinates $\xi = r + z$ and $\eta = r - z$ define two directions of uncoupled motion. Ionisation corresponds to the electron escape in the η-direction only, while the ξ-motion always remains a bound one. The ionisation rate of the Lo Surdo-Stark sublevels thus depends on the potential energy curve drawn along the η-direction only. Because the attraction of the nucleus is not shared between the ξ and η motions in the same way all across the Lo Surdo-Stark manifold, the ionisation rate is not uniquely defined by the total energy.

A more complete description of the discrete Lo Surdo-Stark spectrum of hydrogen calls for the introduction of additional parameters [9]. The one we will keep is the parabolic quantum number n_1, which is the number of nodes the always bound ξ-wave function has between its classical turning points. Quantum number n_1 can be used to label the sub-levels of every n-manifold. More recent studies [10] have aimed at explaining not only the positions but also the shapes (n, n_1) lines or resonances exhibit in the Lo Surdo-Stark spectra [11–13].

The Lo Surdo-Stark effect however does not only affect the discrete part of atomic spectra. The continuum states, and the way they can be reached, *e.g.* in a photoionisation process, are also modified by the electric field. The effect came to observation in a photoionisation experiment of Rb atoms, in the presence of electric fields in the range of a few 10^5 V m^{-1} [14]. Essentially the photoionisation cross-section exhibited an oscillation, as a function of energy, even in an energy region above the zero-field ionisation threshold where nothing was to be seen with zero field but a flat, structureless, continuum. Despite of higher experimental difficulties, the same phenomenon was also

[a] e-mail: blondel@sun.lac.u-psud.fr

observed on hydrogen [12,13], which confirmed the existence of new structures to be observed in the ionisation continuum in the presence of external electric fields.

The point is that even above the zero-field ionisation limit, the parabolic quantum number n_1 remains a good quantum number. The observed modulation of the photoionisation cross-section is actually a series of broad, overlapping n_1 resonances [15], the energy spacing of which rates as $F^{3/4}$ [16,17]. The modulation can also be understood as an interference phenomenon, a one-dimensional picture of which can give proper orders of magnitude. The excited electron can escape the atom with either a positive or a negative velocity v_z. In the former case, since it has a negative electric charge $-q$, it will be reflected by the electric field F towards negative z-values. Interference between the trajectories, that can be either constructive or destructive, depending on the excitation energy, results in a modulation of the ionisation cross-section.

Even in the presence of a strong electric field however, ionisation of an atom is not a one-dimensional problem. If we suppose the detection surface to be a plane of equation $z = -z_0$, the ionisation current has to be expressed as a surface integral of the current density j_z that crosses this plane. Dependence of j_z on the transverse coordinates x and y, or, for symmetry reasons, just on the transverse radius $R = \sqrt{x^2 + y^2}$ yields a complete interference pattern, that can be calculated semi-classically [18]. Moreover, if the observation distance z_0 is much larger than the diameter of the electron spot, which, as will appear further, is always the case in real experiments, the detection surface can be considered as a part of the paraboloid of equation $\eta = 2z_0$. The detector thus directly reproduces the variations of the squared modulus of the detached electron wave function as a function of the orthogonal coordinate ξ only. Since variables ξ and R are related by $\xi \cong R^2/2z_0$ the ξ-function, as seen along the R variable, will undergo a magnification proportional to $\sqrt{z_0}$. A large enough detection distance can thus bring the nodes and antinodes of the atomic electron's wave function to direct observation. This is the principle of the "photoionisation microscope" [19].

Making a photoionisation microscope has yet been impeded by a peculiarity of the Lo Surdo-Stark problem. The expected number of rings in a photoionisation microscopy experiment at the energy of the zero-field ionisation limit is approximately $n_1 = 0.787F^{-1/4} - 1/2$ (with F in atomic units) [9]. On the other hand, the spot has a classical radius R_{cl} which is determined by the classical turning point of the ξ motion, $\xi_{cl} \leq 2F^{-1/2}$. Hence $R_{cl} \approx 2\sqrt{z_0}F^{-1/4}$. The order of magnitude of the interval between adjacent rings will be $i \approx R_{cl}/n_1 \cong 2.5\sqrt{z_0}$ in atomic units, *i.e.* $i \approx 2.5\sqrt{a_0 z_0}$, with a_0 the Bohr radius.

At a distance of one metre, which is already a large one, i is thus of the order of 18 μm only, which is too small to let the interference pattern be directly imaged on an electron detector. As a remarkable fact, i is independent of the applied electric field F, which means that varying F cannot even be of any help. Replacement of the neutral atom by a negative ion yet opens a way to more favorable orders of magnitude, as explained below.

2 The free-electron and point-like emission approximations

Negative ions, especially when one considers their excited states, have a structure entirely different from the structure of neutral atoms. Whereas the motion of a highly excited electron in an atom is dominated by the Coulomb attraction of the positively charged core, the excited electron of a negative ion is a nearly free one. The neutral core of a negative ion acts only as a very localized perturber, which is able to support only a limited number of bound states. In most cases, these states all stem from the same electron configuration, which implies that they all have identical parities. Cesium was considered as a possible exception, but recent experiments in Cs^- [20] dismissed the existence of odd bound states. With the only remaining possible exception of La^- [21], the lowest electric-dipole transition in a negative ion is always to the detachment threshold, into the continuum.

Because of the finiteness of the core effects, a good approximation for the continuum states in a negative ion is to consider them as states of a completely free electron. The corresponding wave-functions are plane waves, hence the equivalent names "plane wave-" or "free electron-" to call this approximation. Electric dipole selection rules will eventually make the free spherical waves more appropriate energy eigenfunctions for the final state, but the approximation remains the same.

In this approximation, the final electron wavelength λ tends to infinity when the excitation energy ε with respect to the detachment threshold goes to zero. There will thus always be an energy domain, in the vicinity of $\varepsilon = 0$, for which the initial wave-function looks like a pinpoint distribution to the final one. Transition probability in this domain will be proportional to the presence probability given by a free spherical wave in a small volume around the origin. This gives the Wigner law [22] for partial detachment cross-sections: $\sigma_\ell \propto \varepsilon^{\ell+1/2}$, with ℓ the orbital angular momentum of the outgoing electron. This simple picture can be somehow complicated by core polarisation effects [23], but given the accuracy of total cross-section measurements, the Wigner law usually provides a quite correct description of the partial cross-section energy dependence up to about 10^{-2} eV above the first detachment threshold [24,25]. The Wigner law is more easily perturbed when higher thresholds are concerned [26], or when photodetachment resonances can be found close to threshold [27].

The Wigner law does not, in principle, tell what the balance between different ℓ channels should be. Meanwhile, the $\ell+1/2$ exponent of this power law clearly shows the importance of the centrifugal barrier the final wave-function has to penetrate to overlap the initial state. As a result of this centrifugal effect, detachment at very low energies always has a nearly 100% branching ratio into the

channel of lowest allowed ℓ value. For instance, when the initial ion and the resulting neutral atom have opposite parities, single-photon detachment close to threshold will always result in the emission of a nearly pure s-wave.

Motion of the detached electron from a negative ion can thus be treated by two very powerful approximations. The electron is emitted from a point source, and its motion ignores the presence of a neutral atomic core remaining at the origin. Within these two approximations, when detachment is produced in the presence of a uniform electric field, the motion of the outgoing electron is exactly analogous to the free fall a massive particle undergoes in the presence of a uniform acceleration field. This is not a problem of classical ballistics however, because the particle is not initially emitted in a state of well-defined initial velocity, but in the form of a completely coherent, isotropic spherical wave.

Free fall seldom has to be considered quantum-mechanically. Yet the question arose about atoms trapped in a gravitational cavity [28], for trapping a sufficiently large number of cold enough atoms could have been a way to achieve high degeneracy factors. The motion of atoms that bounce on a parabolic evanescent wave mirror actually is a separable one, along the already defined parabolic coordinates ξ and η. The origin of the coordinates, in this case, is the mirror focus. However, in contradistinction to the detachment problem, nothing compels the atom's wave function to yield an important presence probability at the focus. On the other hand, because the atoms bounce on the mirror, their η wave-function has to be a stationary one, while the detached electron wave, in this direction, is a progressive one.

Within a homogeneous electric field F, as in free fall [28], a characteristic wavelength λ_0 can be defined for the quantum motion:

$$\lambda_0 = \left(\frac{\hbar^2}{2mqF}\right)^{1/3}. \tag{1}$$

The initial kinetic energy ε of the detached electron can be measured by another distance: $a = \varepsilon/qF$, which is the maximum distance the electron can travel upfield before being reflected.

Imaging the electron distribution, when the electron has been emitted by a point-like source, is nearly taking a direct section of the Green function $G_{ret}(\mathbf{r}, \mathbf{0}; \varepsilon)$ of the problem. Two reduced variables can be used to cover the energy and nearly all of the spatial variations of the Green function, namely

$$\alpha_+ = -\frac{2a+\eta}{2\lambda_0} \quad \text{and} \quad \alpha_- = -\frac{2a-\xi}{2\lambda_0}\,. \tag{2}$$

The Green function is the Fourier transform of the propagator $K(\mathbf{r}, \mathbf{0}; t)$ for a particle in a constant external field. This is the simplest case in mechanics after the completely free particle problem. A newly published demonstration [29], following earlier calculations [30], has now established that G_{ret} can be written in exact analytical form:

$$G_{ret}(\mathbf{r}, \mathbf{0}; \varepsilon) = \frac{m}{2\hbar^2}\frac{1}{r}\left[\mathrm{Ci}(\alpha_+)\mathrm{Ai}'(\alpha_-) - \mathrm{Ci}'(\alpha_+)\mathrm{Ai}(\alpha_-)\right] \tag{3}$$

where $\mathrm{Ai}(u)$ is the regular Airy function, *i.e.* the solution of the one-dimensional Schrödinger equation with a linear potential $V(u) = u$; $\mathrm{Ci}(u) = \mathrm{Bi}(u) + i\mathrm{Ai}(u)$ with Bi the irregular solution of the same equation [31]. Arguments α_+ and α_-, can also be defined, using parameter

$$\beta = \frac{1}{2qF\lambda_0} = \left[\frac{m}{(2\hbar qF)^2}\right]^{1/3},$$

in a more compact way, as $\alpha_+ = -\beta qF(2a+\eta)$ and $\alpha_- = -\beta qF(2a-\xi)$, respectively [29].

From formula (3), one understands that the classical motion is restricted to the domain where both arguments α_+ and α_- have negative values. Since η is always positive, α_+ can only be smaller than $-a/\lambda_0$. The η-motion is thus unrestricted and the η-wave-function, in accordance with the asymptotic behaviour of the Ci and Ci′ functions, is always a progressive wave which just carries the electron away from the point source. We suppose this progressive wave to be totally absorbed by the detector.

The ξ-motion, on the other hand, is always of stationary nature. It has a classical turning point for a maximum value of α_- equal to zero, *i.e.* at $\xi = 2a$. As a consequence, no classical trajectory can reach the detector at a distance R from the axis greater than $R_{cl} = 2\sqrt{a(a+z_0)}$, which is the classical radius of the electron spot.

The order of magnitude of the experimental parameters makes some approximations possible. The excitation energy ε will never be larger than 0.3 meV, the field F will never be smaller than 100 $\mathrm{V\,m^{-1}}$, so a will never be greater than 3 μm, which makes it a negligible quantity with respect to z_0, itself about 0.51 m. Within an excellent approximation the classical radius can thus be written

$$R_{cl} \cong 2\sqrt{az_0}. \tag{4}$$

For electrons falling on the detector at R-values smaller than R_{cl}, we may also write $r = \sqrt{z_0^2 + R^2} \cong z_0 + R^2/2z_0$. We check in this way that the detection plane, in which $\eta \cong 2z_0 + R^2/(2z_0)$, can be considered as a surface of nearly constant η, at $\eta = 2z_0$. This does not matter so much anyway, for the progressive Ci and Ci′ wave factors that formula (3) contains change their modulus but very slowly as functions of η.

As a consequence, the maximum value that $|\alpha_+|$ reaches, in the detection plane, is about z_0/λ_0. For a field $F = 100$ $\mathrm{V\,m^{-1}}$ we have $\lambda_0 \cong 72$ nm. The ratio will thus always be of the order of a few 10^6. Having a very large $|\alpha_+|$ makes it possible to simplify formula (3); because asymptotically $|\mathrm{Ci}'(\alpha_+)/\mathrm{Ci}(\alpha_+)| \cong |\alpha_+|^{1/2}$, the first term of the Green function becomes very small with respect to the second one. At large distances from the ion, within a

good approximation:

$$|G_{ret}(\mathbf{r},\mathbf{0};\varepsilon)|^2 \cong \frac{m^2}{4\pi\hbar^4}\frac{1}{r^2}|\alpha_+|^{1/2}\mathrm{Ai}^2(\alpha_-) = \frac{m^2}{4\pi\hbar^4}\frac{1}{r^2}\sqrt{\frac{z_0}{\lambda_0}}\mathrm{Ai}^2\left[\beta qF(-2a+\xi)\right]. \quad (5)$$

Because r is nearly constant in the detection plane, the wave-function of the electron emitted by the point source essentially exhibits radial variations due to the Ai^2 factor. Since $\xi \cong R^2/2z_0$, these variations can be written

$$j_z \propto \mathrm{Ai}^2\left[\beta qF(-2a+\xi)\right] \cong \mathrm{Ai}^2\left[\frac{1}{\lambda_0}\left(\frac{R^2}{4z_0}-a\right)\right]. \quad (6)$$

The recorded photoelectron image should thus show an oscillatory intensity, *i.e.* a ring pattern, as a function of R up to $R = R_{cl}$, then an exponentially decreasing tail in the dynamical tunneling region [29] beyond R_{cl}. The maximum absolute value of the argument $|\alpha_-| = 2\beta\varepsilon$ is reached at the centre of the image. Though it is not necessarily a large ratio, one can write what the asymptotic expression of the Airy function would yield for the current density

$$j_z \propto \frac{1}{\sqrt{1-\dfrac{R^2}{R_{cl}^2}}}\left[1+\cos\left(\frac{4}{3}|\alpha_-|^{3/2}-\frac{\pi}{2}\right)\right]. \quad (7)$$

In a classical description photodetachment could be described as the incoherent scattering of the electron's charge density uniformly on a expanding sphere. Projection of such a spherical charge distribution, after some definite time (of fall) t, on the detector plane by the electric field would give a $\left[1-(R/R_{cl})^2\right]^{-1/2}$ plane distribution. This is actually what we find for the current envelope. The singularity at $R = R_{cl}$ does not exist in the actual quantum world, for the asymptotic formula does not hold when the argument of the Airy function tends to zero. Nevertheless, the first maximum of the Airy function, closest to $\alpha_- = 0$, is the largest one, so one can expect that every electric-field directed electron image will still exhibit an outer bright ring around $R = R_{cl}$. In the semi-classical interpretation, this can be attributed to the degeneracy of classical trajectories at this radius, in a way analogous to a rainbow effect.

The quantity $(4/3)|\alpha_-|^{3/2}$ is the phase difference that can be calculated semi-classically [18,29]. The additional phase shift results from the wave reflection on the turning surface $\xi = 2a$. The simplicity of the photodetachment problem comes from the fact that only two trajectories lead from the origin to a detection point. Modulation of the photoelectron angular distributions in multiphoton detachment experiments can also be interpreted as resulting from two-trajectory electron interferences [32].

3 Proper orders of magnitude for photodetachment microscopy

The principles of photodetachment microscopy, as described in the previous section, apply at any values of the energy ε and of the applied field F. Observation of the characteristic ring pattern will however be possible only if correct orders of magnitude are given to a few quantities. First of all, a ring pattern will look as a ring pattern only if the number of rings, calculated after (6):

$$N \cong \frac{2}{3\pi}\left|\frac{a}{\lambda_0}\right|^{3/2} \quad (8)$$

is larger than 2. Coming back to the experimental parameters ε and F, the inequality can be written

$$\varepsilon > \left(\frac{3\pi}{\sqrt{2}}\right)^{3/2}\frac{(\hbar qF)^{2/3}}{m^{1/3}} = \frac{(3\pi)^{2/3}}{2}\beta^{-1}. \quad (9)$$

On the other hand, the ring interval must be larger than the expected spatial resolution i_{min} of the electron detection system. Since the mean ring interval i is again just the ratio of the classical radius $R_{cl} \cong 2\sqrt{az_0}$ and the number of rings N, the resolution criterion $i > i_{min}$ will read:

$$3\pi\frac{\sqrt{z_0\lambda_0^3}}{a} > i_{min}$$

i.e.

$$\varepsilon < \frac{3\pi}{\sqrt{2}}\frac{\hbar}{i_{min}}\left(\frac{z_0qF}{m}\right)^{1/2}. \quad (10)$$

Setting the energy ε so that it be smaller than a $F^{1/2}$ law and greater than a $F^{2/3}$ law is always possible, whatever the coefficients, provided one sets the electric field F to small enough values. Unfortunately, electrostatic shielding can never be achieved in a perfect way, in an actual experiment, so making relatively uniform electric fields will likely be a difficult task below 1 $\mathrm{V\,m^{-1}}$.

The major limitation in the direction of small fields however comes from the finite resolution the excitation scheme sets on the energy parameter ε. Actually recorded electron patterns, such as those shown further, appear as the convolution of monoenergetic images by a Gaussian distribution with a width parameter Δ such that $h^{-1}\Delta \cong 900$ MHz. The classical radius R_{cl} of the image varies as the square root of the energy, so this energy convolution induces some additional smoothing on the outer edge of the electron spot. But the main effect of energy broadening is on the maximum phase shift, or number of rings N, which, after (8), varies as a power 3/2 of the energy. Differentiating formula (8) and requiring that the contrast of the most internal rings be attenuated by no more than an e factor, we obtain as a third condition:

$$\varepsilon < \frac{1}{2}\frac{(\hbar qF)^2}{m\Delta^2} = \frac{1}{8\Delta^2\beta^3}. \quad (11)$$

Since all three inequalities deal with power laws of the parameters, they can be conveniently represented on a log-log ε *vs.* F diagram, as done in Figure 1 for the actual experimental conditions, requiring that $i_{min} = 100$ μm. The figure makes it clear that the electric field to be used

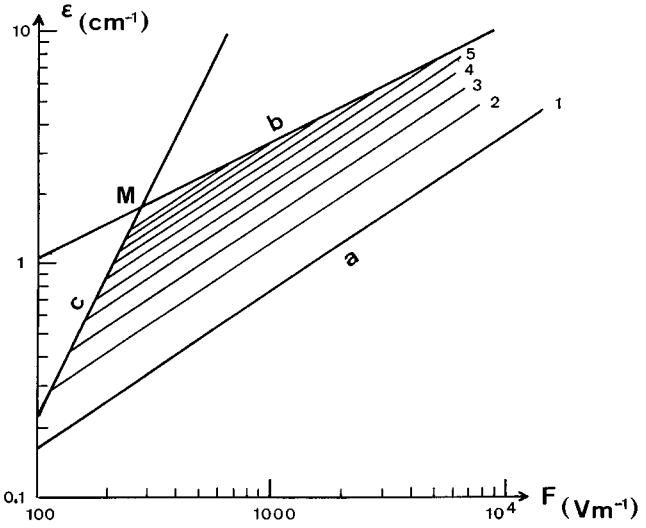

Fig. 1. Log-log diagram of the energy *vs.* electric field domain which makes photodetachment microscopy feasible. The $F^{2/3}$ low limit (a) corresponds to the emergence of the first-order constructive interference maximum. Other parallel isophase lines are labeled according to the expected number of bright rings. The $F^{1/2}$ limit (b) sets a mean ring interval larger than 0.1 mm at a detection distance $z_0 = 0.51$ m. The left limit (c) is given by the condition that the ring pattern not be blurred by an energy resolution $h^{-1}\Delta = 900$ MHz. Point M is where the maximum number of bright rings will be visible, as a compromise between spatial and spectral blurring.

has to be greater than 100 V m^{-1}, with an optimum value of about 300 V m^{-1}, which leads to the best compromise between spatial and spectral blurring. This is represented by point M in Figure 1, at which the number of electron rings that remain distinct has its maximum value

$$N_{max} \approx \left[12\pi \frac{\hbar^2 z_0^2}{m\Delta i_{min}^4}\right]^{1/3} \cong 12. \qquad (12)$$

We have used electric field values in the range 100–500 V m^{-1}. Since the maximum number N_{max} of distinct rings decreases but slowly with the field, larger fields can be considered, but electric fields greater than 1 kV m^{-1} will start accelerating the negative ions substantially, thus making the experiment more difficult. As a consequence, suitable values ε of the excitation energy will be such that the excess excitation wavenumber $\delta = \sigma - \sigma_0$ be in the 0.3–3 cm^{-1} range. The way to achieve these experimental conditions is described in the next chapter.

4 Experimental set-up

The first real photodetachment microscope [33] made use of Br^- ions. The idea was that since halogen negative ions only have complete electron shells, their fundamental level is a non-degenerate one, so negative halogen photodetachment actually starts from a unique quantum state. This indisputable advantage is counterbalanced by the existence of a hyperfine splitting of the neutral ^{79}Br or ^{81}Br ground state, the order of magnitude of which is a few GHz [34], still too small to give the images obtained for different final states distinguishably different R_{cl} radii, but large enough to smooth the experimental modulation of $j_Z(R)$ considerably.

But in the simple model that we have just given, isotropy of the electron detachment pattern only relies on the hypothesis that the electron be initially emitted in the form of an *s*-wave. Uniqueness of the ground state of the negative ion is thus of secondary importance, provided that the electron be brought to such a unique final state. Thanks to the Wigner law, any negative ion the parity of which is opposite to the neutral atom's parity can be used, and a lot of natural isotopes will be found that have no hyperfine structure.

The even isotopes of natural oxygen $^{16}O^-$ and $^{18}O^-$ obey both criteria. A beam of O^- ions is easily produced from a hot cathode discharge source, fed with a mixture of argon (80%) and N_2O (20%). The source as a whole is set at a voltage of −1200 volts with respect to the body of the experimental chamber. Pure oxygen, either of the 16 or the 18 isotope, is selected through a Wien velocity filter, set about 25 cm in front of the source. The O^- beam goes through a series of diaphragms, lenses, steering plates, a quadrupole 90°deflector, which eliminates collisionally produced neutral atoms, and a decelerator that brings the kinetic energy of the ions down to 500 eV, before entering the interaction region.

A schematic view of the interaction region and microscopy chamber is given by Figure 2. At the exit of the decelerator, about 8 cm before the interaction region, a last skimmer of diameter 1.3 mm makes the ion beam as clean as possible. The beam, as measured from the photodetachment images themselves, has a diameter of about 0.6 mm. Though several nA of pure $^{16}O^-$ going through the interaction chamber can easily be achieved, better results are obtained when the current is intentionally reduced to 200 pA or less. This can be the sign of space charge effects. The latter value actually corresponds to limiting the space charge electric field, on the surface of the ion beam, to less than 0.15 V m^{-1}. This is a small, but may be not completely negligible fraction of the externally applied, uniform electric field. Since ion current limitation is achieved not only by closing diaphragms, but also by reducing the source running currents, the improvement may also be due to better working conditions of the source itself. Better conditions mean that the ion velocity and, as a consequence, Doppler effect dispersions are made smaller in the experimental sample.

The electric field is vertical. It is produced by a pile of 28 stainless steel parallel plates, with a central hole of 27 mm in diameter. The thickness of the plates decreases to 0.5 mm at their inner brim, so as not to perturb the field uniformity in the central region. Voltage setting of the plates is made with 0.1% precision division resistances, that directly connect each plate to the adjacent one, inside the vacuum chamber. Adjacent plates around the interaction region are separated by 14 mm intervals and

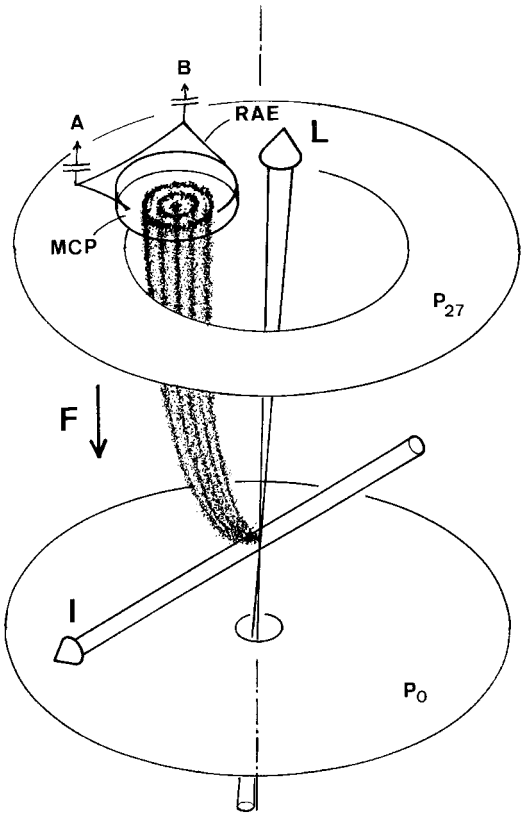

Fig. 2. Scheme of the experimental set-up, showing the expansion of the electron wave-function from the photodetachment zone up to the high spatial resolution detector. L is the laser, I the ion beam, P_0 and P_{27} are the two extreme plates, 28 in total number, that produce the uniform electric field F. The stack of micro-channel plates MCP, is followed by a resistive anode encoder RAE, partially drawn, two of the four outputs of which are shown, A and B, going to the position analyzer.

connected through 100 kΩ resistors, whereas in the further part of the uniform-field region, the period is extended to 21 mm and the connection made through 150 kΩ resistors.

The electric field being downwards directed, electrons are detected at the top of the uniform field column. In a field the minimum value of which is 100 $\mathrm{V\,m^{-1}}$, an electron undergoes an upward acceleration always greater than 1.7×10^{13} $\mathrm{m\,s^{-2}}$. Gravity, in our experimental conditions, is thus negligible [35]. The whole uniform-field region is shielded against the Earth magnetic field by a double layer of 0.8 mm thick mu-metal.

The detector [36] consists of a series of $2 + 3$ micro-channel plates (MCP's) followed by a resistive anode encoder. For every event, the electric pulses emitted *via* the four corners of the anode are first pre-amplified, then compared in order to determine the mean position of the electron bunch produced by the last MCP. The position at which the parent incident electron arrived on the detector can be determined in this way with a dispersion less than 63 μm FWHM. For proper operation, electrons are supposed to arrive at the detector sequentially, which is the case in a CW laser photodetachment experiment, as the present one, but would not be true if photodetachment was produced by a pulsed laser. The maximum counting and position encoding rate of the detector is 6×10^4 $\mathrm{s^{-1}}$, far above the actual photoelectron production from the negative ion beam, in the 10–10^4 $\mathrm{s^{-1}}$ range.

The spatial resolution of the electron images results from a convolution of the intrinsic resolution of the detector with additional, extrinsic, causes. The most important one is the width of the interaction volume, *i.e.* the intersection of the ion and laser beams, which produces a dispersion of the initial position of the detached ion in the directions orthogonal to the electric field. Focusing the detachment laser can help to reduce this width, provided that the laser beam has been made parallel, or quasi-parallel to the field. Since no mirror can be set in front of the detector, and since the detector operation would probably be perturbed by a direct impact of the laser, the laser beam is set to pass just outside of the detector, *i.e.* not vertically but at a 3° angle from the electric field, in the common plane of both the ion beam and electric field. This adds a slight loss of spatial resolution in the direction of the ion flight, of the order of an additional 15 μm half-width. A corresponding sharpness anisotropy of the electron ring pattern is visible in the experimental images, that are shown below. More important however is the isotropic broadening due to the width of the laser spot, the waist parameter of which we estimated to be 19.2 μm.

The photodetachment threshold of O^- is known from previous laser photodetachment experiments [37]. The corresponding threshold wavenumber is admitted to be 11 784.648(6) $\mathrm{cm^{-1}}$ [38]. In this near-infrared spectral region, the excitation light is provided by a single mode sapphire-titanium laser system, which delivers about 1 W of light power onto the ion beam. The photodetachment cross-section being less than 10^{-23} $\mathrm{m^2}$ [39], ions that spend typically 0.2 ns under the corresponding illumination, namely 7×10^{27} photons $\mathrm{s^{-1}m^{-2}}$, will have a detachment probability lower than 2×10^{-5}. In spite of the high intensity of the CW laser, detachment thus remains in a completely linear regime.

The laser wavenumber is measured by means of a lambdametre, which permanently compares the laser wavelength to the one of a stabilized He–Ne laser. Applying the standard correction for the ratio of the air indices at 633 and 848 nm, we obtain the wavenumber of the detaching photon with an accuracy of $\pm\, 2 \times 10^{-3}$ $\mathrm{cm^{-1}}$, *i.e.* $\pm\, 2$ mk. The frequency shift of the laser while an image is being recorded, *i.e.* for 600 to 5000 s, remains within these limits.

The spectral line can be considered as monochromatic with respect to the large Doppler broadening it undergoes when seen from the ions' rest frame. For ions that cross with a velocity v a laser focus with a waist parameter w_0, the apparent photon energy gets an additional Gaussian half-width $\Delta = \sqrt{2}\hbar v / w_0$. Actual data show the effective width Δ to be such that $h^{-1}\Delta \cong 900$ MHz, *i.e.* 30 mk in wavenumber units. This is exactly what the latter formula yields for 500 eV $^{16}O^-$ ions, with a velocity $v = 77\,\mathrm{km\,s^{-1}}$,

that cross a $w_0 = 19.2$ μm waist. The effective energy width of the exciting photon is thus mainly due to laser focusing.

One should not forget, however, that the essential role of laser focusing is to keep the spatial resolution good enough to make the ring pattern visible. Formula (12) can finally be used to put together the advantages and drawbacks of laser focusing. As long as the size of the laser focus can be considered as the limiting factor for the spatial resolution, N_{max} will scale as w_0^{-1}. Making w_0 as small as possible is thus the good way to obtain the largest possible number of visible rings, as long as the overall spatial resolution can benefit from stronger focusing. The optimum value is met when w_0 has become of the same order, or slightly smaller than the electron detector spatial resolution. Since the latter is about 31 μm (half-width), $w_0 = 19.2$ μm can be considered as a good setting.

5 Photodetachment images

Figure 3 shows a series of photodetachment images that have been recorded with the same $F = 423\ \mathrm{V\,m^{-1}}$ value of the electric field. One can check with the naked eye that the number of rings N increases faster and faster, and the radius R_{cl} more and more slowly, when the energy ε increases. The explanation comes directly from formulae (4, 8), which show that N increases as $\varepsilon^{3/2}$, whereas R_{cl} only varies as $\varepsilon^{1/2}$. One can thus directly observe how the rings become narrower, hence less distinct, when one goes to higher energies, or how one drops into the less-than-one-ring regime for too small values of ε.

Slight distortions are observed, as a slight departure from the perfect circular shape. The fact that the smaller the nominal field F, the larger the distortion strongly suggests that it may be due to the presence of some additional, non-uniform, electric field or to imperfect shielding of the magnetic field. To take the effect into account, fitting the recorded images by formula (6) is made allowing the square of the nominal radius R to be a more general quadratic function of the X and Y coordinates of the detector, *i.e.* allowing the rings to be ellipses, all with the same eccentricity.

As could be expected due to the deviation of the laser beam from perfect parallelism with the field, the observed spatial blurring is also non isotropic. This is essentially visible through the regular non-uniformity of the illumination, all around every bright ring, that can be clearly reproduced through two-dimensional fitting (Fig. 4). Other deviations from a uniform illumination can be observed, that result from the non-uniform response of the detector. This is the consequence of the local fatigue of the MCP's, as a function of the integrated current every channel has delivered. Different zones of the detector can be used, from one image to the other, by changing the position of the laser and ion beam intersection, in order make the effects of MCP fatigue more uniform.

When the ellipticity of a recorded image is known, the information it contains can be put together in a one-dimensional radial histogram. Averaging strongly reduces

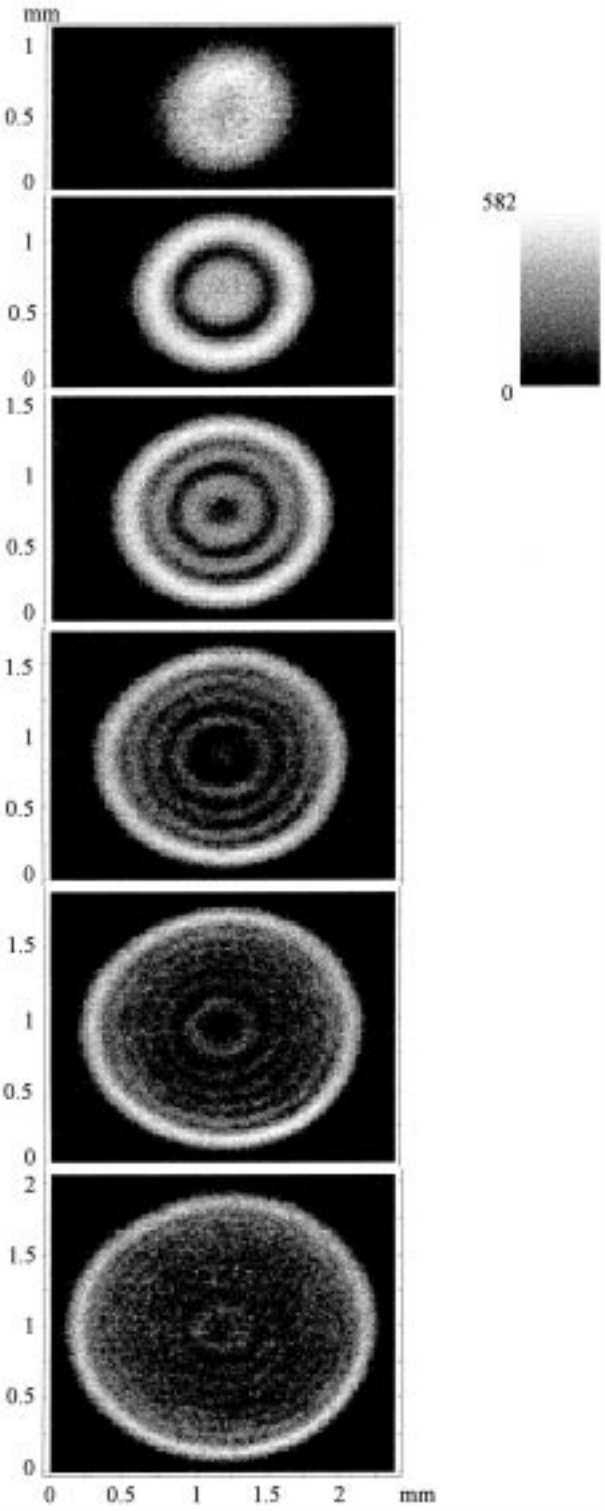

Fig. 3. Photodetachment microscopy images of $^{16}O^-$ within a 423 $\mathrm{V\,m^{-1}}$ electric field, for excitation energies 0.26, 0.535, 0.811, 1.089, 1.367, and 1.654 $\mathrm{cm^{-1}}$ (from top to bottom) above the detachment threshold. These energy values do not make use of the wavelength measurement, nor of any absolute size measurement on the images, but they result from fitting the images with the theoretical formula for the ring pattern. Acquisition time was 600 s for the first image, 700 s for the others.

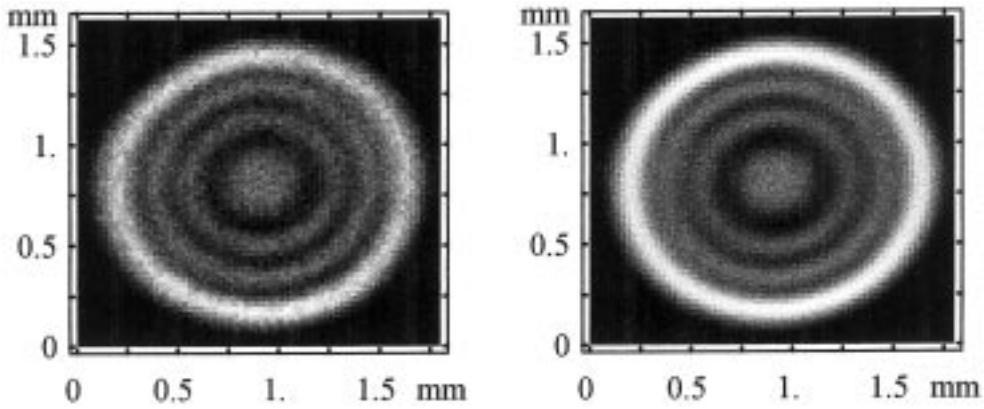

Fig. 4. A photodetachment image taken in the same experimental conditions as for the previous series, but at an intermediate detachment energy $\varepsilon = 0.951$ cm^{-1}. The synthetic, fitting image presented on the right makes the spatial resolution anisotropy more visible. The direction along which the image appears as elongated and the principal direction of increased blurring are adjusted independently but they come to be nearly the same with an angular difference of 0.1 rad only. Relying on the wavenumber measurement of the exciting laser, $\sigma = 11\,785.594(2)$ cm^{-1} and on the admitted value of the electron affinity, $11\,784.648(6)$ cm^{-1}, we can use the fitted energy $\varepsilon = 0.951$ cm^{-1} to estimate the angle by which the ion and laser beam cross together. The result is $90.09(16)^\circ$, consistent with the experimental beam orientations.

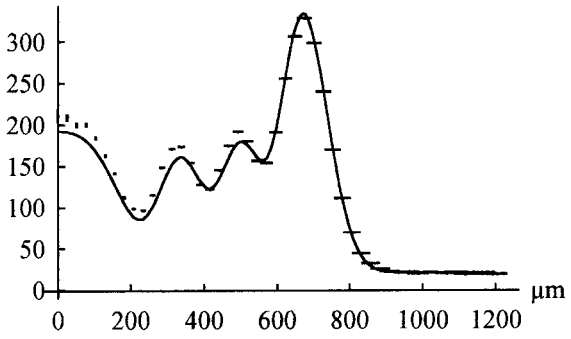

Fig. 5. The radial histogram of the number of counted electrons per pixel, for the very image shown in Figure 4. Ellipticity of the ring pattern has been taken into account by the two-dimensional fitting procedure, but the exact pixel size is not known exactly, which results in an uncertainty on the abscissae that increases proportionally to the abscissae themselves. On the other hand, the larger the radius, the more pixels are found at this radius, and the more the averaging procedure reduces the counting fluctuations. The 21 electrons/pixel background is not noise, but a uniform illumination background due to 20 and 178 cm^{-1} electrons detached from fine structure-excited O^-, with neutral O left in its excited $^3P_1$ or ground $^3P_2$ state, respectively.

the statistical fluctuations of the number of counted electrons per pixel, as can be seen in Figure 5. A systematic deviation is observed, that brings the calculated inner rings always below, and the outer bright ring always above the experimental data. The way this slight relative discrepancy varies with the absolute counts makes it consistent with a non-linearity or fatigue effect occurring during the recording.

The essence of the fitting procedure, since we have images that look more like interferograms than classical ballistic distributions, is to rely on phase, rather than on radius measurements, in order to determine the experimental energy ε. Formula (6) is thus used as a fitting formula with a and the actual dimensions of the image as free parameters. The total phase $2\pi N$, which is unambiguous, will settle the energy measurement *via* the a/λ_0 ratio, according to formula (8). The main advantage of the procedure is that no assumption on the actual size of the image is necessary. This is fortunate, since the pixels are not real pixels, their definition only result from the analog-to digital conversion of the X- and Y-position signals, the ratios of which can vary with the electronics settings. In addition, the phase brings a better sensitivity to energy variations than plain dimension measurements, because of the $\varepsilon^{3/2}$ *vs.* $\varepsilon^{1/2}$ laws the two quantities obey, according to formulae (8, 4) respectively.

Yet determining the energy *via* phase measurements completely relies on the validity of (6). Despite of the given reasons for the validity of the pinpoint source and free-electron approximations, the photodetachment microscope could well work as a phase-contrast microscope for the half of the electron wave that passes twice over the neutral core, the unreflected half serving as the phase reference. Even small rescattering effects by the neutral core [40] could thus become visible. A systematic deviation of the recorded images from the zeroth-order approximation represented by formula (6) must be considered.

As a test of such a possible deviation, we have plotted in Figure 6 the measured energy ε, as a function of the excitation wavenumber, for the whole series of 423 V m^{-1} detachment images. No anomaly is observed that would suggest that ε is not the actual ejection energy of the detached electron. We can thus conclude that photodetachment of O^- within electric fields of a few 10^2 V m^{-1}, at energies not exceeding 2 cm^{-1} above threshold, is actually free from rescattering by the oxygen neutral core. In such experimental conditions, the obtained images can be

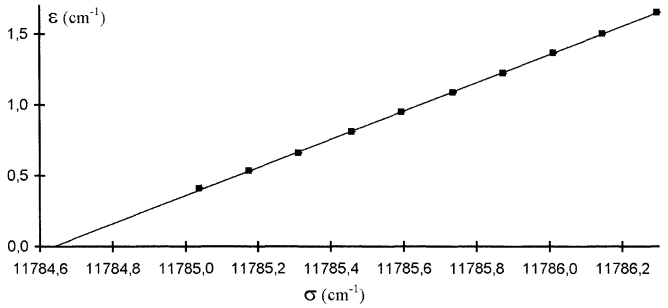

Fig. 6. Plot of the measured initial kinetic energy ε, as produced by the fitting procedure, as a function of the laser wavenumber σ. If the fitting procedure is correct, when both quantities are expressed in the same unit (here cm^{-1}) the points should lie along a straight line of slope 1, and the extrapolated abscissa for $\varepsilon = 0$ should yield the known value of the electron affinity of oxygen. All three criteria are obeyed perfectly, within the limits set by the experimental uncertainties.

considered as reference images, as if they had been produced with free electrons emitted by a real point source.

6 Conclusion

The conclusion we can draw from the last result is, to some extent, paradoxical. On the one hand, what we have brought to observation is the stationary factor of the continuum wave function of atomic O^-. It is a direct view of an atomic wave function, which gives unprecedented insight into the radial motion an electron can have around an atomic nucleus. On the other hand, quantitative analysis of the result shows that the observed wave-function finally has very little atomic character. It is just the intensity image of the quantum propagator of any massive particle, when submitted to a uniform acceleration field. Such a situation could also be described by the transformation of a free expanding wave to a uniformly accelerated frame, and looked at from a relativistic point of view [41].

Oxygen however is a small atom. The situation may well change when looking at photodetachment images of a similar but bigger ion such as S^-, the photodetachment interference of which has already been observed as a modulation of the total detachment cross-section [42]. The case of identical parities of the parent ion and residual atom can also offer an additional degree of freedom, for the low energy odd electron escapes in a p-wave. Both radial and angular distributions in the photodetachment images are then expected to depend on the laser polarisation [43,44]. Again, the images may be interpreted as cross-sections of an electronic Green function, the multipole Green function $G_{\ell m}(\mathbf{r}, \mathbf{0}; \varepsilon)$ generated by an oriented point source with dipole angular characteristics [45].

The electron microscope itself could benefit from the rapid progress made by photo-electron imaging, that was also developed in a regime of purely classical mechanics for electron spectrometry and angular measurement purposes [46]. In such experiments, blurring by too wide electron sources is also a problem, that was circumvented by making the photo-electrons pass through three different longitudinal electric fields before they reach the detector. With properly set, such a combination acts as an immersion lens, from which the electrons that have been emitted with equal velocities reach a common position on the detector [47]. Whether such a "velocity mapping" technique could apply to photodetachment microscopy strongly depends on how the relative phase of interfering trajectories will be perturbed when passing through electrostatic lenses, in conditions of only approximate stigmatism.

Replacing the uniform electric field by a series of properly set electrostatic lenses also makes it possible to achieve some image magnification. This could be a way to make neutral atom photoionisation microscopy feasible, without having to built a one hundred metre long experimental chamber. For an electron that goes away from an ionic core, classical trajectories are much more complicated than in the detachment case [48], and the interference, from a semi-classical point of view, can be of higher orders than a simple two-wave one. The photoionisation microscope could thus bring out some phenomena that have no equivalent in the photodetachment case, such as glory effects [49], in addition to the familiar rainbow that we see in photodetachment images as the accumulation circle at $R = R_{max}$.

We gratefully acknowledge abundant correspondence with C. Bracher. It was again a pleasure to discuss about photoionisation and photodetachment microscopy with V.N. Ostrovskii. Discussions with M. Jaekel and S. Reynaud helped us to see the problem from another point of view, and gave us interesting additional references. We also thank I. Yu. Kiyan for his participation at an early stage of the experiment and P.A. Golovinskii for many discussions during his stay at L.A.C.

References

1. A. Lo Surdo, Atti della Reale Accademia dei Lincei, Rendiconti **22**, 664 (1913).
2. J. Stark, Nature **92**, 401 (1913); Sitz. Ber. der K. Preuss. Ak. der Wiss. **47**, 932 (1913).
3. E. Schrödinger, *Abhandlungen zur Wellenmechanik* (Johann Ambrosius Barth, Leipzig, 1927).
4. P.M. Koch, D.R. Mariani, Phys. Rev. Lett. **46**, 1275 (1981).
5. C. Delsart, L. Cabaret, C. Blondel, R.-J. Champeau, J. Phys. B: At. Mol. Phys. **20**, 4699 (1987).
6. R.J. Damburg, V.V. Kolosov, J. Phys. B: At. Mol. Phys. **12**, 2637 (1979).
7. H.A. Bethe, E.E. Salpeter, *Quantum mechanics of one- and two-electron atoms* (Springer Verlag, Berlin, 1957).
8. L.D. Landau, E.M. Lifchitz, *Kvantovaya Mekhanika* (Nauka, Moskva, 1974); *Mécanique quantique* (Mir, Moscou, 1974); *Quantum Mechanics* (Pergamon, Oxford, 1977); *Quantenmechanik* (Akademie-Verlag, Berlin, 1979).
9. D.A. Harmin, Phys. Rev. A **24**, 2491 (1981).
10. G. Alvarez, R.J. Damburg, H.J. Silverstone, Phys. Rev. A **44**, 3060 (1991).

11. T. Bergeman, C. Harvey, K.B. Butterfield, H.C. Bryant, D.A. Clark, P.A.M. Gram, D. MacArthur, M. Davis, J.B. Donahue, J. Dayton, W.W. Smith, Phys. Rev. Lett. **53**, 775 (1984).
12. W.L. Glab, M.H. Nayfeh, Phys. Rev. A **31**, 530 (1985).
13. H. Rottke, K.H. Welge, Phys. Rev. A **33**, 301 (1987).
14. R.R. Freeman, N.P. Economou, G.C. Bjorklund, K.T. Lu, Phys. Rev. Lett. **41**, 1463 (1978).
15. E. Luc-Koenig, A. Bachelier, Phys. Rev. Lett. **43**, 921 (1979); J. Phys. B: At. Mol. Phys. **13**, 1743 (1980); J. Phys. B: At. Mol. Phys. **13**, 1769 (1980).
16. A.R.P. Rau, J. Phys. B: At. Mol. Phys. **12**, L193 (1979); Comments At. Mol. Phys. **10**, 19 (1980).
17. V.D. Kondratovich, V.N. Ostrovskii, Zh. Eksp. Teor. Fiz. **79**, 395 (1980) [Sov. Phys. JETP **52**, 198 (1980)].
18. I.I. Fabrikant, Zh. Eksp. Teor. Fiz. **79**, 2070 (1980) [Sov. Phys. JETP **52**, 1045 (1980)].
19. Yu.N. Demkov, V.D. Kondratovich, V.N. Ostrovskii, Pis'ma Zh. Eksp. Teor. Fiz. **34**, 425 (1981) [JETP Lett. **34**, 404 (1981)].
20. M. Scheer, J. Thøgersen, R.C. Bilodeau, C.A. Brodie, H.K. Haugen, H.H. Andersen, P. Kristensen, T. Andersen, Phys. Rev. Lett. **80**, 684 (1998).
21. S.H. Vosko, J.B. Lagowski, I.L. Mayer, J.A. Chevary, Phys. Rev. A **43**, 6389 (1991).
22. E.P. Wigner, Phys. Rev. **73**, 1002 (1948).
23. T.F. O'Malley, Phys. Rev. **137**, A1668 (1965).
24. H. Hotop, W.C. Lineberger, J. Phys. Chem. Ref. Data **14**, 731 (1985).
25. D. Calabrese, A. Covington, J.S. Thompson, R.W. Marawar, J.W. Farley, Phys. Rev. A **54**, 2797 (1996).
26. P.G. Harris, H.C. Bryant, A.H. Mohagheghi, R.A. Reeder, H. Sharifian, C.Y. Tang, H. Tootoonchi, J.B. Donahue, C.R. Quick, D.C. Rislove, W.W. Smith, J.E. Stewart, Phys. Rev. Lett. **65**, 309 (1990).
27. J.R. Peterson, Y.K. Bae, D.L. Huestis, Phys. Rev. Lett. **55**, 692 (1985).
28. H. Wallis, J. Dalibard, C. Cohen-Tannoudji, Appl. Phys. B **54**, 407 (1992).
29. C. Bracher, W. Becker, S.A. Gurvitz, M. Kleber, M.S. Marinov, Am. J. Phys. **66**, 38 (1998). A slight difference may however appear with these authors' formulae, due to an opposite convention about the sense of the electric field. In order to keep the same orientation as in most Lo Surdo-Stark descriptions [7–10,16,17,28], we shall suppose the electric field F to be oriented towards positive z-values. Keeping the same formal definition of parabolic coordinates, we thus logically obtain an inversion of ξ and η. The physical results, such as the radial distribution of photoelectron current, are of course unaffected.
30. F.I. Dalidchik, V.Z. Slonim, Zh. Eksp. Teor. Fiz. **70**, 47 (1976) [Sov. Phys. JETP **43**, 25 (1976)].
31. M. Abramowitz, I.A. Stegun, *Handbook of mathematical functions* (Dover Publications, New York, 1972).
32. G.F. Gribakin, M.Yu. Kuchiev, Phys. Rev. A **55**, 3760 (1997); J. Phys. B: At. Mol. Opt. Phys. **30**, L657 (1997).
33. C. Blondel, C. Delsart, F. Dulieu, Phys. Rev. Lett. **77**, 3755 (1996).
34. G.H. Fuller, V.W. Cohen, Nucl. Data Tab. A **5**, 433 (1969); G.H. Fuller, J. Phys. Chem. Ref. Data **5**, 835 (1976).
35. In an actual experiment, the free electron under study is not the only thing subject to gravity. The free electrons flowing in the surrounding metallic electrodes also undergo their own weight. Because of the nearly total electrical influence between the one and the others, the detached electron, if the electric field was cancelled, would be more in a gravity-less situation than in free fall. Experiments that intended to measure the weight of electrons flying inside Faraday cages actually faced this curious zero-weight result. See T.W. Darling, F. Rossi, G.I. Opat, G.F. Moorhead, Rev. Mod. Phys. **64**, 237 (1992) and references therein, especially F.C. Witteborn, W.M. Fairbank, Phys. Rev. Lett. **19**, 1049 (1967).
36. Model 3391 of Quantar Technology Inc., 3004 Mission street, Santa Cruz, CA 95060, USA.
37. D.M. Neumark, K.R. Lykke, T. Andersen, W.C. Lineberger, Phys. Rev. A **32**, 1890 (1985).
38. C. Blondel, Phys. Scripta T **58**, 31 (1995).
39. G. Miecznik, C.H. Greene, Phys. Rev. A **53**, 3247 (1996).
40. I.I. Fabrikant, J. Phys. B: At. Mol. Opt. Phys. **27**, 4545 (1994).
41. M.-T. Jaekel, S. Reynaud, Eur. Phys. J. (submitted, 1998).
42. N.D. Gibson, B.J. Davies, D.J. Larson, Phys. Rev. A **47**, 1946 (1993).
43. M.L. Du, Phys. Rev. A **40**, 4983 (1989)
44. P.A. Golovinskii, Zh. Eksp. Teor. Fiz. **112**, 1574 (1997) [JETP **85**, 857 (1997)].
45. C. Bracher, to be submitted for publication.
46. H. Helm, N. Bjerre, M.J. Dyer, D.L. Huestis, M. Saeed, Phys. Rev. Lett. **70**, 3221 (1993); H. Helm, M.J. Dyer, Phys. Rev. A **49**, 2726 (1994); C. Bordas, J.C. Pinaré, Phys. Rev. A **57**, R681 (1998).
47. A.T.J.B. Eppink, D.H. Parker, Rev. Sci. Instrum. **68**, 3477 (1997); D.H. Parker, A.T.J.B. Eppink, J. Chem. Phys. **107**, 2357 (1997).
48. C. Bordas, Phys. Rev. A **58**, 400 (1998).
49. V.D. Kondratovich, V.N. Ostrovsky, J. Phys. B: At. Mol. Opt. Phys. **23**, 3785 (1990).